AIAA 00–2552

Validation of Several Reynolds-Averaged Turbulence Models in a 3-D Unstructured Grid Code

James R. Forsythe
Department of Aeronautics
United States Air Force Academy

William Z. Strang
Air Force Research Laboratory
Computational Sciences Branch

Klaus A. Hoffmann
Department of Aerospace Engineering
Wichita State University

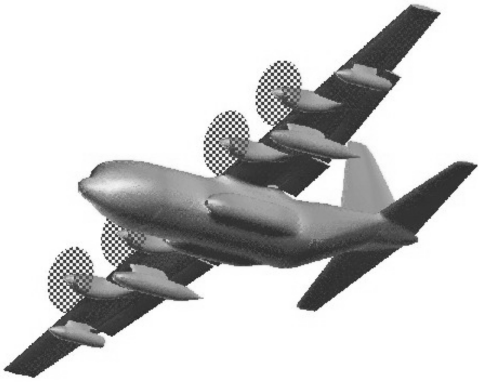

Fluids 2000
19–22 June 2000 / Denver, CO

For permission to copy or republish, contact the American Institute of Aeronautics and Astronautics
1801 Alexander Bell Drive, Suite 500, Reston, VA 20191–4344

Validation of Several Reynolds-Averaged Turbulence Models in a 3-D Unstructured Grid Code

James R. Forsythe*
Department of Aeronautics
United States Air Force Academy

William Z. Strang†
Air Force Research Laboratory
Computational Sciences Branch

Klaus A. Hoffmann‡
Department of Aerospace Engineering
Wichita State University

The Wilcox 1998 k-ω, Menter's baseline, and Menter's shear stress transport turbulence models have been incorporated in *Cobalt*$_{60}$ — an unstructured grid, finite volume, parallel, implicit code. Previously, *Cobalt*$_{60}$ included the one-equation Spalart-Allmaras and Baldwin-Barth models. The Wilcox 1998 k-ω turbulence model includes many advanced features, such as: compressibility corrections, transition modeling, round jet corrections and a cross diffusion term. The round jet corrections and cross diffusion terms were introduced by Wilcox in 1998. One weakness of the k-ω model, however is sensitivity to freestream conditions for shear layer flows. Menter's models blend the k-ϵ and k-ω equations to alleviate this problem. Menter added the shear stress transport correction which has had a great deal of success accurately predicting boundary layer separation. Menter's models, however, do not contain compressibility or round jet corrections. Suzen and Hoffmann investigated adding compressibility corrections and round jet corrections to the k-ϵ portion of Menter's models. These corrections are investigated in the present study. All models are subjected to a wide range of test cases to validate proper implementation, robustness, model performance, and accuracy issues on triangular grids. Comparison is made to empirical data, other computational studies, and experimental data.

Introduction

REYNOLDS-AVERAGED Navier-Stokes (RANS) turbulence models are commonly used for engineering applications. There are numerous RANS turbulence models, and more are introduced each year. The reason that there are so many is that there is not one model that can solve all flows accurately. It is therefore of utmost importance to understand the strengths and weaknesses of each model. Any Navier Stokes code should also have several models to choose from (in this authors opinion), with complementary strengths. It is tempting to write a code with a single model, in a black box approach. However, the lack of universality of RANS models does not currently support this approach.

Cobalt$_{60}$ is an unstructured grid, implicit, parallel Euler/Navier-Stokes solver developed at Air Force Research Laboratory, Computational Sciences Branch (see Strang et al. [1], Grismer et al. [2], Tomaro et al. [3]). Unstructured grids are used, because the code is intended for heavy engineering use. Grids can be created using VGRIDns and GRIDTOOL [4] around full aircraft (such as the F-18, SR-71, F-16, etc.) within one week. Previously, *Cobalt*$_{60}$ employed the one-equation models of Spalart-Allmaras [12] and Baldwin-Barth [6]. Algebraic models were not considered, due to complications in implementation for an unstructured grid. The Spalart-Allmaras model is a particularly strong model for aircraft applications. It is able to predict separation under adverse pressure gradients with a good amount of accuracy. However,

---

*Assistant Professor, Member AIAA

†Aerospace Engineer

‡Professor, Associate Fellow AIAA

it does not have compressibility corrections for high speed shear layers. The model has trip functions, where the user defines locations on the geometry where transition is believed to occur. This an improvement over models without this capability, but the capability within *Cobalt*$_{60}$ is often not used because of the difficulty of picking these locations over a full 3D geometry. Another disadvantage of the Spalart-Allmaras model is that it requires a wall distance, which can be very expensive to compute for an unstructured grid.

Because of the above weaknesses of the Spalart-Allmaras model, and to provide more choices to users, it was decided to add two-equation models to *Cobalt*$_{60}$. Additionally, the Baldwin-Barth model was removed due to poor performance. The new models added were Menter's shear stress transport (SST) and baseline (BSL) models [7] as well as Wilcox's 1998 version of the k-ω model [5]. Menter's shear stress transport has enjoyed a great deal of success in separated flows and is insensitive to freestream values of ω (see [9]). It does, however, require a wall distance to be calculated. Wilcox's k-ω model, on the other hand, does not require wall distance. Wilcox [5] in 1998 added a cross diffusion term and a round jet correction to the k-ω model to improve shear layer predictions. The k-ω model also has low-Reynolds number corrections that attempt to predict transition without any user intervention. Finally, compressibility corrections are added that increase the accuracy for high-speed shear layers, without polluting the boundary layer solution. Although the original Menter's models did not contain compressibility corrections, Suzen and Hoffmann [17] proposed adding corrections to the k-ϵ portion of the model. These corrections were further tested by Forsythe et al. [8].

Currently the 1998 k-ω model is completely coded into *Cobalt*$_{60}$, however the round jet and low-Reynolds-number corrections are disabled, as will be discussed in the Turbulence Models section. The Menter's models have the compressibility corrections of Suzen and Hoffmann [17] included. Results will be presented with and without these corrections. The release version of the code will have the corrections active.

The goal of the present study is a comprehensive validation of the new and existing models in *Cobalt*$_{60}$. The validation process encompasses implementation, robustness, model performance, and accuracy issues on triangular grids. To validate the implementation of the models, comparisons are made to other computational studies and the boundary layer code of Wilcox [5]. Robustness is tested on all problems by running the code at a CFL number of one million. Model performance is validated by applying all models to a wide range of problems including transonic shock separation, supersonic compression ramp separation, a supersonic jet, and supersonic base flows. Comparisons are made with experimental data in all these cases. Finally, a comparison between quadrilateral and triangular grids is made on several of the flows to assess the impact of using highly stretched triangles (or tetrahedrons in 3D).

Governing Equations

The Euler and Navier-Stokes equations are solved in an inertial reference frame. In integral form, the Navier-Stokes equations are

$$\frac{\partial}{\partial t}\iiint_{\mathcal{V}} Q\,d\mathcal{V} + \iint_{\mathcal{S}} (f\hat{\imath} + g\hat{\jmath} + h\hat{k})\cdot\hat{n}\,d\mathcal{S} = \iint_{\mathcal{S}} (r\hat{\imath} + s\hat{\jmath} + t\hat{k})\cdot\hat{n}\,d\mathcal{S} \quad (1)$$

where

$$Q = \begin{bmatrix}\rho\\ \rho u\\ \rho v\\ \rho w\\ \rho e\end{bmatrix} \qquad f = \begin{bmatrix}\rho u\\ \rho u^2 + p\\ \rho uv\\ \rho uw\\ u(\rho e + p)\end{bmatrix}$$

$$g = \begin{bmatrix}\rho v\\ \rho uv\\ \rho v^2 + p\\ \rho vw\\ v(\rho e + p)\end{bmatrix} \qquad h = \begin{bmatrix}\rho w\\ \rho uw\\ \rho vw\\ \rho w^2 + p\\ w(\rho e + p)\end{bmatrix}$$

The viscous stresses are:

$$r = \begin{bmatrix}0\\ \tau_{xx}\\ \tau_{xy}\\ \tau_{xz}\\ a\end{bmatrix} \qquad s = \begin{bmatrix}0\\ \tau_{xy}\\ \tau_{yy}\\ \tau_{yz}\\ b\end{bmatrix} \qquad t = \begin{bmatrix}0\\ \tau_{xz}\\ \tau_{yz}\\ \tau_{zz}\\ c\end{bmatrix}$$

Here $a = u\tau_{xx} + v\tau_{xy} + w\tau_{xz} + kT_x$, $b = u\tau_{xy} + v\tau_{yy} + w\tau_{yz} + kT_y$, and $c = u\tau_{xz} + v\tau_{yz} + w\tau_{zz} + kT_z$; $\mathcal{V}$ is the fluid element volume; $\mathcal{S}$ is the fluid element surface area; $\hat{n}$ is the outward-pointing unit normal to $\mathcal{S}$; $\hat{\imath}$, $\hat{\jmath}$, and $\hat{k}$ are the Cartesian unit vectors; ρ is the density; p is the pressure; u, v, and w are the velocity components; e is the specific energy per unit volume; T is the temperature; k is the thermal conductivity; and τ_{xx}, τ_{yy}, τ_{zz}, τ_{xy}, τ_{xz}, and τ_{yz} are the viscous stress tensor components. The ideal-gas law and Sutherland's law close the system of equations and the entire equation set is non-dimensionalized by freestream density and speed of sound.

The semi-discrete form of the equations is:

$$\mathcal{V}_i\frac{dQ_i}{dt} + \sum_{M=1}^{N_i}(f^M\hat{\imath} + g^M\hat{\jmath} + h^M\hat{k})\cdot\hat{n}^M\mathcal{S}^M = \sum_{M=1}^{N_i}(r^M\hat{\imath} + s^M\hat{\jmath} + t^M\hat{k})\cdot\hat{n}^M\mathcal{S}^M \quad (2)$$

where the subscripted i and superscripted M denote quantities for the i^{th} cell and the M^{th} face of cell i, respectively, and N_i is the number of faces bounding cell i.

To model the effects of turbulence, a turbulent viscosity (μ_t) is calculated, as described below. To obtain k_t, a turbulent Prandtl number is assumed (0.9) with the following relation: $\mathrm{Pr}_t = \frac{c_p \mu_t}{k_t}$. In the governing equations, μ is replaced by $(\mu + \mu_t)$ and k is replaced by $(k + k_t)$.

Cobalt$_{60}$ can solve the above equations for 3D, 2D, or 2D axisymmetric problems. For the current study the code was run in either 2D or 2D axisymmetric modes.

Turbulence Models

Spalart-Allmaras One-Equation Model

The Spalart-Allmaras one-equation model [12] solves a single partial differential equation for a variable $\widetilde{\nu}$ which is related to the turbulent viscosity. The differential equation is derived by "using empiricism and arguments of dimensional analysis, Galilean invariance and selected dependence on the molecular viscosity." The model includes a wall-destruction term that reduces the turbulent viscosity in the laminar sublayer and trip terms that provide a smooth transition from laminar to turbulent flow. The differential equation is

$$\begin{aligned}\frac{D\widetilde{\nu}}{Dt} &= c_{b1}\left(1 - f_{t2}\right)\widetilde{S}\,\widetilde{\nu} \qquad (3)\\ &+\frac{1}{\sigma}\left[\nabla\cdot\left(\left(\nu+\widetilde{\nu}\right)\nabla\widetilde{\nu}\right) + c_{b2}\left(\nabla\widetilde{\nu}\right)^2\right]\\ &-\left[c_{w1}f_w - \frac{c_{b1}}{\kappa^2}f_{t2}\right]\left[\frac{\widetilde{\nu}}{d}\right]^2 + f_{t1}\Delta U^2\end{aligned}$$

where the turbulent viscosity is determined by

$$\begin{aligned}\nu_t &= \widetilde{\nu} f_{v1} &(4)\\ f_{v1} &= \frac{\chi^3}{\chi^3 + c_{v1}^3} &(5)\\ \chi &= \frac{\widetilde{\nu}}{\nu} &(6)\end{aligned}$$

S is the magnitude of the vorticity, and the modified vorticity is

$$\begin{aligned}\widetilde{S} &= S + \frac{\widetilde{\nu}}{\kappa^2 d^2} f_{v2} &(7)\\ f_{v2} &= 1 - \frac{\chi}{1 + \chi f_{v1}} &(8)\end{aligned}$$

where d is the distance to the closest wall. The wall destruction function f_w is

$c_{b1} = 0.1355$	$\sigma = \frac{2}{3}$	$c_{b2} = 0.622$	$\kappa = 0.41$
$c_{w1} = \frac{c_{b1}}{\kappa^2} + \frac{(1+c_{b2})}{\sigma}$	$c_{w2} = 0.3$	$c_{w3} = 2$	$c_{v1} = 7.1$
$c_{t1} = 1$	$c_{t2} = 2$	$c_{t3} = 1.1$	$c_{t4} = 2$

Table 1 Spalart-Allmaras model coefficients

$$\begin{aligned}f_w &= g\left[\frac{1 + c_{w3}^6}{g^6 + c_{w3}^6}\right]^{\frac{1}{6}} &(9)\\ g &= r + c_{w2}(r^6 - r) &(10)\\ r &= \frac{\widetilde{\nu}}{\widetilde{S}\kappa^2 d^2} &(11)\end{aligned}$$

Large values of r are truncated to 10. The trip functions are:

$$\begin{aligned}f_{t2} &= c_{t3}\exp\left(-c_{t4}\chi^2\right) &(12)\\ f_{t1} &= c_{t1} g_t \exp\left(-c_{t2}\frac{\omega_t^2}{\Delta U^2}\left[d^2 + g_t^2 d_t^2\right]\right) &(13)\end{aligned}$$

where d_t is the distance from the field point to the trip (on the wall), ω_t is the wall vorticity at the trip, ΔU is the difference between the velocity at the field point and that at the trip, and $g_t \equiv min\left(0.1, \frac{\Delta U}{\omega_t \Delta x}\right)$ where Δx is the grid spacing along the wall at the trip point. The closure coefficients are given in Table 1.

Modifications

The only modification made in *Cobalt*$_{60}$ to the standard Spalart-Allmaras model described above is a simplification to the trip terms. Instead of using Equation 13 which is expensive to calculate, a large value of $\widetilde{\nu}$ is specified at the trip locations. For the current calculations, however, the computations were fully turbulent, so the trip functions were set to zero (i.e. $C_{t3} = 0$). The model is designated **SA** for all figures.

Wilcox 1998 k-ω Model

Wilcox [5] revised the original k-ω model in 1998 to include terms to give a more accurate spreading rate for round and radial jets, as well as planar shear layers. The k-ω model solves a transport equation for turbulent kinetic energy (k) and turbulent specific dissipation rate (ω).

$$\begin{aligned}\frac{D}{Dt}(\rho k) &= \tau_{ij}\frac{\partial u_i}{\partial xj} - \beta^* \rho\omega k &(14)\\ &+\frac{\partial}{\partial x_j}\left[\left(\mu + \sigma^*\mu_t\right)\frac{\partial k}{\partial x_j}\right]\\ \frac{D}{Dt}(\rho\omega) &= \alpha\frac{\omega}{k}\tau_{ij}\frac{\partial u_i}{\partial xj} - \beta\rho\omega^2 &(15)\\ &+\frac{\partial}{\partial x_j}\left[\left(\mu + \sigma\mu_t\right)\frac{\partial \omega}{\partial x_j}\right]\end{aligned}$$

Where the turbulent shear stress is

$\alpha_\infty = \frac{13}{25}$	$\alpha^*_\infty = 1$	$\sigma = \frac{1}{2}$	$\sigma^* = \frac{1}{2}$
$\beta_i = \beta_0 f_\beta$	$\beta^*_\infty = \beta^*_0 f_{\beta^*}$	$\beta_0 = \frac{9}{125}$	$\beta^*_0 = \frac{9}{100}$

Table 2 Wilcox k-ω incompressible, fully turbulent model coefficients

$\alpha^*_0 = \frac{\beta_i}{3}$	$\alpha_0 = \frac{1}{9}$	$Re_T = \frac{k}{\omega\nu}$
$R_\beta = 8$	$R_k = 6$	$R_\omega = 2.95$

Table 3 Wilcox k-ω low-Reynolds-number model coefficients

$$\tau_{ij} = \alpha^* \left[\mu_t \left(\frac{\partial u_i}{\partial x_j} + \frac{\partial u_j}{\partial x_i} - \frac{2}{3} \frac{\partial u_k}{\partial x_k} \delta_{ij} \right) - \frac{2}{3} \rho k \delta_{ij} \right] \tag{16}$$

and the turbulent viscosity is found from

$$\mu_t = \rho \frac{k}{w} \tag{17}$$

Incompressible, fully turbulent parameters are given in Table 2.

The round jet and cross-diffusion corrections added in 1998 are

$$f_\beta = \frac{1 + 70\chi_\omega}{1 + 80\chi_\omega} \quad \chi_\omega = \left| \frac{\Omega_{ij}\Omega_{jk}S_{ki}}{(\beta^*_0 \omega)^3} \right| \tag{18}$$

$$f_{\beta^*} = \begin{cases} 1, & \chi_k \le 0 \\ \frac{1+680\chi_k^2}{1+400\chi_k^2}, & \chi_k > 0 \end{cases} \qquad \chi_k = \frac{1}{\omega^3} \frac{\partial k}{\partial x_j} \frac{\partial \omega}{\partial x_j} \tag{19}$$

Wilcox includes low-Reynolds number corrections to simulate and predict transition. If the low-Reynolds number corrections are not included, then

$$\alpha^* = \alpha^*_\infty \quad \alpha = \alpha_\infty \quad \beta^*_i = \beta^*_\infty \tag{20}$$

If low-Reynolds-number corrections are included

$$\begin{aligned} \alpha^* &= \alpha^*_\infty \frac{\alpha^*_0 + Re_T/R_k}{1 + Re_T/R_k} && (21) \\ \alpha &= \alpha_\infty \frac{\alpha_0 + Re_T/R_\omega}{1 + Re_T/R_\omega} \frac{1}{\alpha^*} && (22) \\ \beta^*_i &= \beta^*_\infty \frac{4/15 + (Re_T/R_\beta)^4}{1 + (Re_T/R_\beta)^4} && (23) \end{aligned}$$

where the low-Reynolds-number model coefficients are given in Table 3.

The model includes compressibility corrections to decrease the spreading rates predicted for compressible shear layers. A heavy-sided step function (Equation 26) is used to turn the correction off for boundary layers, where it would otherwise decrease the predicted skin friction. The compressible values of β and β^* are

$$\begin{aligned} \beta &= \beta_i \left[1 - \frac{\beta^*_i}{\beta_i} \xi^* F(M_t) \right] && (24) \\ \beta^* &= \beta^*_i \left[1 + \xi^* F(M_t) \right] && (25) \end{aligned}$$

with the compressibility function

$$F(M_t) = \begin{cases} 0, & M_t \le M_{t0} \\ M_t^2 - M_{t0}^2 & M_t > M_{t0} \end{cases} \tag{26}$$

where

$$\begin{aligned} M_t &= \sqrt{\frac{2k}{a^2}} && (27) \\ M_{t0} &= \frac{1}{4} && (28) \end{aligned}$$

and a is the speed of sound.

Modifications

The 1998 Wilcox model has been coded in its entirety into *Cobalt*$_{60}$. Currently, however, several terms have been turned off, awaiting further testing.

Equation 18 should return $\frac{7}{8}$ for f_β when used on a round jet, and 1.0 otherwise. It was found to give $\frac{7}{8}$, however, even in the M=0.1 boundary layer. The cause for this is unknown at this time, and further testing is needed.

The low-Reynolds-number corrections are also currently deactivated. These corrections were tested on a flat plate boundary layer. Transition would occur downstream on the flat plate, but then it would move gradually upstream until the boundary layer was fully turbulent.

There are several methods of setting boundary conditions for ω on no-slip walls, as discussed in [5]. *Cobalt*$_{60}$ uses the approach taken by Menter [7], which is

$$\omega = \frac{N \nu_w}{(\Delta y_2)^2} \tag{29}$$

where Δy_2 is the distance to the wall of the nearest cell center. Menter suggested a value of 800 for N. In the current study, it was found that the skin-friction results for the flat plate were sensitive to the value of N, and that slightly different values of N were required for the different models (including Menter's models) to match the expected skin friction. Although the difference in skin-friction was only 2-5% with $N = 800$, this sensitivity should be explored further.

The Wilcox model as described is designated as **KW** in all figures. In one case the compressibility correction is turned off (i.e. $\xi^* = 0$), and is designated as

KW-NOCC. In another case, the round jet (or axisymmetric) correction is turned on, and is designated as **KW-A**.

Menter's k-ϵ/k-ω Models

Wilcox's k-ω is well behaved in the near wall region where low-Reynolds-number corrections are not required. However, it is generally very sensitive to the freestream values of ω. On the other hand, the k-ϵ equations are relatively insensitive to freestream values, but behave poorly in the near wall region [9]. This sensitivity seems to be a factor mainly for free shear flows and does not seem to adversely affect boundary layer flows.

Menter [7, 10, 11] proposed a combined k-ϵ, k-ω model which uses the best features of each model. The model uses a parameter F_1 to switch from k-ω to k-ϵ in the wake region to prevent the model from being sensitive to freestream conditions. The governing differential equations are

$$\begin{aligned}
\frac{D}{Dt}(\rho k) &= \tau_{ij}\frac{\partial u_i}{\partial x_j} - \beta^* \rho \omega k \\
&\quad + \frac{\partial}{\partial x_j}\left[(\mu + \sigma_k \mu_t)\frac{\partial k}{\partial x_j}\right] \qquad (30)\\
\frac{D}{Dt}(\rho \omega) &= \frac{\gamma \rho}{\mu_t}\tau_{ij}\frac{\partial u_i}{\partial x_j} - \beta \rho \omega^2 \\
&\quad + \frac{\partial}{\partial x_j}\left[(\mu + \sigma_\omega \mu_t)\frac{\partial \omega}{\partial x_j}\right] \\
&\quad + 2\rho(1 - F_1)\sigma_{\omega 2}\frac{1}{\omega}\frac{\partial k}{\partial x_j}\frac{\partial \omega}{\partial x_j} \qquad (31)
\end{aligned}$$

To compute the switching function, F_1:

$$\arg_1 = \min\left(\max\left(\frac{\sqrt{k}}{0.09\omega y}; \frac{500\mu}{\rho \omega y^2}\right); \frac{4\rho\sigma_{\omega 2} k}{CD_{k\omega} y^2}\right) \qquad (32)$$

$$CD_{k\omega} = \max\left[2\rho\sigma_{\omega 2}\frac{1}{\omega}\frac{\partial k}{\partial x_i}\frac{\partial \omega}{\partial x_i}; 10^{-20}\right] \qquad (33)$$

$$F_1 = \tanh\left(\arg_1^4\right) \qquad (34)$$

The switching function also determines the value of the model constants. If ϕ_1 represents a generic constant of the k-ω equations, and ϕ_2 represents the same constant for the k-ϵ equations, then the model constants used in Equations 30 and 31 are determined by:

$$\phi = F_1\phi_1 + (1 - F_1)\phi_2 \qquad (35)$$

Set 1 (k-ω)

$\sigma_{k1} = 0.5$	$\sigma_{\omega 1} = 0.5$	$\beta_1 = 0.0750$
$\beta^* = 0.09$	$\kappa = 0.41$	$\gamma_1 = \frac{\beta_1}{\beta^*} - \frac{\sigma_{\omega 1}\kappa^2}{\sqrt{\beta^*}}$

Set 2 (k-ϵ)

$\sigma_{k2} = 1.0$	$\sigma_{\omega 2} = 0.856$	$\beta_1 = 0.0828$
$\beta^* = 0.09$	$\kappa = 0.41$	$\gamma_2 = \frac{\beta_2}{\beta^*} - \frac{\sigma_{\omega 2}\kappa^2}{\sqrt{\beta^*}}$

Table 4 Menter's Baseline model coefficients

Set 1 (k-ω)

$\sigma_{k1} = 0.85$	$\sigma_{\omega 1} = 0.5$	$\beta_1 = 0.0750$
$\beta^* = 0.09$	$\kappa = 0.41$	$\gamma_1 = \frac{\beta_1}{\beta^*} - \frac{\sigma_{\omega 1}\kappa^2}{\sqrt{\beta^*}}$

Set 2 (k-ϵ)

$\sigma_{k2} = 1.0$	$\sigma_{\omega 2} = 0.856$	$\beta_1 = 0.0828$
$\beta^* = 0.09$	$\kappa = 0.41$	$\gamma_2 = \frac{\beta_2}{\beta^*} - \frac{\sigma_{\omega 2}\kappa^2}{\sqrt{\beta^*}}$

Table 5 Menter's Shear Stress Transport model coefficients

Baseline Model

The Baseline model uses the following relation to determine the turbulent viscosity:

$$\mu_t = \rho\frac{k}{\omega} \qquad (36)$$

The Baseline model constants are given in Table 4.

Shear Stress Transport

The Shear Stress Transport model was developed to increase the model's accuracy for separated flows. This model limits the turbulent shear stress to $\rho a_1 k$ where $a_1 = 0.31$. The turbulent viscosity is therefore given by

$$\mu_t = \frac{\rho a_1 k}{\max(a_1\omega; \Omega F_2)} \qquad (37)$$

where Ω is the absolute value of vorticity. The function F_2 is included to prevent singular behavior in the freestream where Ω goes to zero. F_2 is given by

$$\begin{aligned}
F_2 &= \tanh\left(\arg_2^2\right) \qquad (38)\\
\arg_2 &= \max\left(2\frac{\sqrt{k}}{0.09\omega y}; \frac{400\nu}{y^2\omega}\right) \qquad (39)
\end{aligned}$$

The model constants were recalibrated, with the only change being in σ_{k1}, as shown in Table 5.

Modifications

Both the Baseline (**BSL**) and the Shear Stress Transport (**SST**) models have been coded into *Cobalt*$_{60}$ as described above. The boundary conditions on ω on no-slip walls is described in the k-ω section.

Menter did not include compressibility corrections in his model. Suzen and Hoffmann [17], however, added compressible dissipation and pressure dilatation terms to the k-ϵ portion of Menter's models. When Menter's blending process is applied, the following equations result:

$$\begin{aligned}\frac{D}{Dt}(\rho k) &= \tau_{ij}\frac{\partial u_i}{\partial x_j} + (1-F_1)\,\overline{p''d''} \\ &- \beta^* \rho \omega k \left(1+\alpha_1 M_t^2 (1-F_1)\right) \\ &+ \frac{\partial}{\partial x_j}\left[(\mu + \sigma_k \mu_t)\frac{\partial k}{\partial x_j}\right]\end{aligned} \tag{40}$$

$$\begin{aligned}\frac{D}{Dt}(\rho \omega) &= \frac{\gamma \rho}{\mu_t}\tau_{ij}\frac{\partial u_i}{\partial x_j} + (1-F_1)\,\beta^* \alpha_1 M_t^2 \rho \omega^2 \\ &+ \frac{\partial}{\partial x_j}\left[(\mu + \sigma_\omega \mu_t)\frac{\partial \omega}{\partial x_j}\right] - \beta \rho \omega^2 \\ &+ 2\rho (1-F_1)\,\sigma_{\omega 2}\frac{1}{\omega}\frac{\partial k}{\partial x_j}\frac{\partial \omega}{\partial x_j} - (1-F_1)\,\frac{\overline{p''d''}}{\nu_t}\end{aligned} \tag{41}$$

where the pressure dilatation term is

$$\overline{p''d''} = -\alpha_2 \tau_{ij}\frac{\partial u_i}{\partial x_j}M_t^2 + \alpha_3 \rho \epsilon M_t^2 \tag{42}$$

and the closure coefficients for the compressible corrections are

$$\alpha_1 = 1.0 \quad \alpha_2 = 0.4 \quad \alpha_3 = 0.2$$

By adding these corrections only to the k-ϵ portions of the model, the near wall solution (k-ω portion) is unaffected, as observed by Forsythe et al. [8]. This is a similar approach the Wilcox's use of the heavy sided step function described previously. These terms have been included in *Cobalt*$_{60}$ and are designated as **BSL-CC** and **SST-CC**.

The k-ϵ equations (which Menter's models reduce to when far from a wall) give reasonable spreading rates for plane jets but overpredict round jet spreading rates [5]. Suzen and Hoffmann [17] added a correction to Menter's models to decrease the spreading rate in round or axisymmetric jets. This correction is simply to change the value of γ_2 to 0.6. To be more useful, there should be a function to switch this correction on only when needed. Perhaps a similar approach to Wilcox's model (Equation 18) could be taken. This could be a subject for future research if the modification shows potential. The correction has been included in the two round jet cases and is designated as **BSL/SST-CCA** and **BSL/SST-A** (with and without compressibility corrections).

Results

Grids

One of the most challenging aspects of unstructured solvers is to calculate viscous solutions on tetrahedron (or triangles in 2D) grids, as discussed by Barth [14]. To explore the accuracy of *Cobalt*$_{60}$ and the turbulence model implementation on triangular grids, the following approach was taken. All grids were created as two-dimensional structured grids using Gridgen. These quadrilateral grids are designated as **Quad**. Then the same grid was triangulated (opposite corners of the quadrilateral were connected). These grids are designated as **Tri**. This makes a direct comparison between a structured and unstructured grid possible. An example of the two grid types is shown in Figure 24. Most grids had a average first y^+ of less than 1.0, and all were less than 2.0.

Convergence

A common convergence criteria used is to ensure that the residuals have dropped by several orders of magnitude. The flux limiter in *Cobalt*$_{60}$, however, turning on and off prevents this from being a useful convergence criteria. Instead, a variety of parameters are monitored. These include integrated forces and moments, number of supersonic cells, and average value of y^+. An example convergence history for the NACA 0012 calculation is shown in Figure 1. Note that in this case, all models are converged in less than 1500 iterations. The SST model converges slower than the other models. This is because currently the implicit Jacobian only includes the dependence of μ_t on other variables if the SST correction is inactive (i.e. $a_1\omega > \Omega F_2$ in Equation 37). Modifying the Jabian to include the case where $a_1\omega < \Omega F_2$ could result in speed improvements, and is a subject for future research.

Flat Plate

All models were applied to a zero-pressure-gradient adiabatic flat plate. An incompressible case ($M = 0.1$) as well as a supersonic case ($M = 2.5$) was examined. A grid-refinement study was performed for the incompressible case. The grid dimensions are designated by the streamwise and spanwise number of points (e.g. 200x100 is the finest grid). Quad and Tri grids were run for both cases. The length of the plate was one meter, with a Reynolds number of 5 million at the end of the plate. The velocity profiles plotted are half-way down the plate (a local Reynolds number of 2.5 million). Before the beginning of the no-slip wall was a small length with a slip wall to allow the inflow boundary conditions to be placed away from the no-slip wall.

Empirical correlations from Hopkins and Inouye [13] are used for comparing skin friction and momentum thickness — designated **Empirical**. First an adiabatic wall temperature is calculated from

$$\frac{T_{aw}}{T_e} = 1 + r\frac{\gamma - 1}{2}M_e^2 \tag{43}$$

with a recovery factor of $r = 0.9$ assumed. A reference temperature is calculated by

$$\frac{T_{ss}^{'}}{T_e} = 1 + 0.035M_e^2 + 0.45\left(\frac{T_{aw}}{T_e} - 1\right) \quad (44)$$

Transformation functions are given by

$$F_c = \frac{T_{ss}^{'}}{T_e} \quad F_\theta = \frac{\mu_e}{\mu_{ss}^{'}} \quad F_x = \frac{F_\theta}{F_c} \quad (45)$$

The incompressible transformed skin-friction and momentum-based Reynolds numbers are taken from

$$\bar{C}_f = 0.088\frac{\log_{10}\overline{Re}_x - 2.3686}{\left(\log_{10}\overline{Re}_x - 1.5\right)^3} \quad (46)$$

$$\overline{Re}_\theta = \frac{0.044\overline{Re}_x}{\left(\log_{10}\overline{Re}_x - 1.5\right)^2} \quad (47)$$

The following transformation relations are used to relate the compressible values to the incompressible

$$\bar{C}_f = F_c C_f \quad \overline{Re}_\theta = F_\theta Re_\theta \quad \overline{Re}_x = F_x Re_x \quad (48)$$

The velocities are first transformed using the Van Driest transformation:

$$\begin{aligned} \frac{u^*}{U_\infty} &= \frac{1}{A}\sin^{-1}\left(A\frac{u}{U_\infty}\right) & (49) \\ A^2 &= \frac{(\gamma-1)}{2}M_\infty^2\frac{T_\infty}{T_w} & (50) \end{aligned}$$

and compared to the law of the wall (with $\kappa = 0.41$ and $B = 5.0$). Results are also compared against the boundary layer code EDDYBL of Wilcox [5]. This code includes the Spalart-Allmaras and k-ω models — designated **SA EDDYBL** and **KW EDDYBL** respectively in the figures.

Figures 2 through 7 present skin-friction and velocity profiles for the $M = 0.1$ case. The Quad grid agrees well with both the empirical correlations and EDDYBL. The k-ω based models on the Tri grid give slightly higher values of skin-friction than expected. This may be related to the sensitivity to the wall boundary conditions on ω discussed previously. It is also possible that because of the extremely large values of ω on the wall, calculating the gradients of ω is difficult on triangular grids. The SA model, on the other hand, is unchanged on the Tri grid. A possible explanation is that $\widetilde{\nu}$ in the SA model decreases linearly to zero towards the wall. Therefore gradients of $\widetilde{\nu}$ are much lower that gradients of ω, and easier to calculate accurately. The law of the wall is well captured on both the Quad and Tri grids (see Figures 6 and 7)

Case	y^+	F_x	% diff
SA 200x100 Quad	0.63	5.561	–
SA 200x80 Quad	1.3	5.587	0.5
SA 200x60 Quad	2.5	5.702	2.5
SA 100x100 Quad	0.63	5.607	0.8
SA 50x100 Quad	0.63	5.93	6.6
SA 200x100 Tri	0.42	5.544	0.3
SA 200x80 Tri	0.83	5.574	0.2
SA 200x60 Tri	1.7	5.512	0.9
SA 100x100 Tri	0.42	5.597	0.6
SA 50x100 Tri	0.42	5.652	1.6
KW 200x100 Quad	0.64	5.646	1.5
KW 200x80 Quad	1.2	5.506	1.0
KW 200x60 Quad	2.5	5.425	2.4
KW 100x100 Quad	0.64	5.69	2.3
KW 50x100 Quad	0.64	5.723	2.9
KW 200x100 Tri	0.45	6.072	9.2
KW 200x80 Tri	0.88	6.052	8.8
KW 200x60 Tri	1.7	6.027	8.4
KW 100x100 Tri	0.45	6.160	10.8
KW 50x100 Tri	0.45	6.243	12.3

Table 6 $M = 0.1$ **Grid Refinement Results - Case, Average y^+, Integrated axial force, and % difference from SA 200x100 Quad.**

Results of the grid refinement study are seen in Figures 4 and 5 an summarized in Table 6. Sensitivity to both streamwise and wall-normal spacing was examined. The SA model was less sensitive wall normal spacing than the KW model but more sensitive to the streamwise spacing. Based on Table 6 it is recommended that y^+ be kept around 1.0 or lower for both models.

Results for the supersonic flat plate are shown in Figures 8 through 11. The noise so clearly evident in the supersonic flat plate triangular grid skin-friction results (Figure 8), and less so in the incompressible flat plate triangular grid results (Figure 3), is due to the discrete representation of $\mathcal{D} = \vec{\nabla} \cdot \alpha \vec{\nabla} q$, where α may be a constant or a variable. From Strang et al. [1], it is required that any discrete representation of $\mathcal{D}$ be conservative and positive, i.e. that it satisfies the discrete maximum principle [14, 15]. A very desirable third attribute of the formulation is that it be "linearity preserving", in that when $\mathcal{D}$ is applied to a linear field, the null result is returned. The simultaneous satisfaction of these three attributes is generally impossible for arbitrary grids [15]. In [1], linearity-preservation was dropped, with no ill effects observed at that time. Since then, however, the numerical errors associated with such an approach have been observed and a rudimentary corrective action has been taken. Observing that the above state of affairs is somewhat similar to construction of second-order accurate and positive inviscid fluxes, we have applied a limiter to $\mathcal{D}$. The basic idea is to use a conservative and linearity-preserving formulation of $\mathcal{D}$, except in those circumstances where the non-positive contributions would indeed cause instability, where the formulation is switched to be conservative and positive. The non-positive contributions are zero for an orthogonal grid, where the unit normal vector for any given face is parallel to the vector between the centroids of the two cells sharing the face.

It is the switching between the two formulations for $\mathcal{D}$ that produces the noise seen in the flat plate results. The larger the gradient of q and the lower the orthogonality of the grid, such as with high-aspect ratio triangles or tetrahedra, the larger the non-positive contributions tend to be, thus exacerbating the problem. The flat plate cases are very sensitive to this problem, where a short portion of a slip wall abruptly transitions into a no-slip wall. Gradients of velocity and ω are very high at the no-slip leading edge, which activates the $\mathcal{D}$-limiter, which in turn causes oscillations down the length of the plate. More realistic geometries, where a leading edge is geometrically modeled and a true stagnation point is captured, infrequently activates the $\mathcal{D}$-limiter and the results are much improved.

A second type of $\mathcal{D}$-limiter has been tried, and the skin-friction results for the supersonic plate were smooth and accurate. However, this $\mathcal{D}$-limiter is unstable for more demanding, realistic three-dimensional geometries. More work is needed in the area of constructing a smooth $\mathcal{D}$-limiter, or in constructing a conservative, positive, *and* linearity preserving formulation of $\mathcal{D}$.

Incompressible Jets

Free shear flows are a basic building-block flow that each turbulence model should handle accurately. Wilcox [5] discusses several free shear flows: far wake, mixing layer, plane jet, round jet, and radial jet. These flows all become self-similar sufficiently far downstream. An important parameter to predict for the jet is the spreading rate δ'. For the jet, this is defined as the value of y/x where the velocity is half of the peak velocity. x is the spanwise distance from the jet exit, and y is the spanwise distance from the jet centerline. Wilcox [5] gives spreading rates for several turbulence models based on solving self-similar equations.

Currently, only the round and plane jets have been examined. Solving the full Navier-Stokes equations for a jet exiting into a quiescent flow (i.e. $M = 0.0$) is a challenge for a compressible code, as seen by Suzen and Hoffmann [17]. Accurate boundary condition treatment is required to prevent reflections. The low Mach numbers can also cause slow convergence. Currently only a satisfactory solution has been obtained for Menter's models – BSL/SST. The SA and KW models failed to reproduce a self-similar solution. Instead, the turbulent viscosity seemed to accumulate in the quiescent region, polluting the solution. Since a satisfactory solution was obtained for the BSL/SST model, it is assumed that the problems are related to the turbulence models themselves, and not the flow solver. Future research will be conducted to obtain results for the other models and solve the other free shear flows.

Flow	BSL/SST (A)	k-ϵ [5]	Measured [5]
Round Jet	0.120 (0.080)	0.120	0.086-0.096
Plane Jet	0.104	0.108	0.100-0.110

Table 7 Spreading rates for the round and plane jets

Figure 12 shows contours of Mach number for the round jet case (BSL/SST). Modified Riemann invariants ($M = 0.0$) were used for all farfield boundary conditions. A slip wall was placed prior to the jet to allow the farfield conditions to be placed away from the jet. The jet exit velocity was $M = 0.3$. The solution is smooth and absent of any reflections from the relatively close farfield boundary conditions. The convergence criteria used was to plot the velocity profiles at several stations to ensure a self-similar solution.

Figure 13 presents the velocity profiles for the round and plane jet. The spreading rates can be found from this figure and are presented in Table 7. Since the Menter's models away from walls are based on the k-ϵ model, results are compared to the k-ϵ model results from [5] and seen to be in good agreement. The model overpredicts the round jet spreading rate, as expected. The axisymmetric correction (BSL/SST-A) lowers the spreading rate, but lowers it too much in comparison with measured values.

Supersonic Round Jet

The supersonic exhaust jet flow of Seiner and Norum [16] is next examined. The experiment examined the flowfield for an underexpanded jet exhausting into a quiescent flow. The jet conditions are $M_j = 2.0$, $p_j/p_\infty = 1.45$, and a temperature ratio of $T_j/T_\infty = 1.0$. The subscript j represents the conditions at the jet exhaust. In their experiment, $p_\infty = 101325\, N/m^2$, $T_\infty = 293\, K$, and the jet exit diameter is $D = 5.08\, cm$. This flow was previously examined by Suzen and Hoffmann [17] with all of the same models, except for KW.

The grid used is presented in Figure 14. The boundary condition treatment was the same as detailed above, except that an inflow Mach number of 0.1 was specified for all models except for BSL/SST, which used 0.001. This approach was taken due to the difficulties found for the other models in the incompressible jet case. The jet exit was specified as a "source" with a uniform Mach number of 2.0. Suzen and Hoffmann [17], on the other hand, used the experimental velocity profile. This may be an explananation for the minor differences seen in the *Cobalt*$_{60}$ solutions and those of [17].

Figure 15 presents pressure along the centerline for

$M_1 = 2.56$	$p_1 = 27566 N/m^2$	$u_1 = 584.13 m/s$
$M_2 = 2.05$	$p_2 = 61110 N/m^2$	$u_2 = 523.85 m/s$

Table 8 2-D Base test conditions

all models, including the axisymmetric corrections to Menter's models and Wilcox's k-ω. The KW model is overdamped. This is surprising in light of the presence of compressibility corrections. This could potentially be due to sensitivity to freestream boundary conditions as discussed in [9]. This possibility should be researched further. The axisymmetric correction improves the results, but the difference from the experimental values is still large. The SA and BSL/SST models are also overdamped, which is not surprising since they lack compressible shear layer corrections. The compressibility corrections to BSL/SST greatly improve the results. Adding the axisymmetric correction (BSL/SST-CCA) provides a more accurate amplitude, but the phase is slightly shifted downstream.

Figure 16 compares results on the Quad grid to the Tri grid. The Tri grid for both models is more damped. This could be due to the limiter on $\mathcal{D}$ turning on because of the combination of high-aspect-ratio triangles and strong gradients. To explore this further, a grid refined in the streamwise direction should be created.

Figure 17 presents the levels of turbulent viscosity for all cases at $x/D = 5.5$. The drastic reduction of μ_t by the compressibility corrections is clearly seen.

2-D Base Flow

The two stream supersonic, turbulent wake flowfield behind a thick base corresponding to the experimental data of Amatucci et al. [23] has been calculated. The flow consists of two uniform supersonic turbulent streams which separate at the corners of a finite thickness base and form a flowfield with characteristics similar to those of a flowfield behind a missile. The properties of the upper (1) and lower (1) streams are given in Table 10, and the total temperature in both cases is 299 K.

The grid used is shown in Figure 18. An artificial "channel" upstream of the base was created to provide the correct boundary layer thickness prior to the base. The length of this channel was determined by running the boundary layer code – EDDYBL [5]. The length was determined by matching the experimental values of momentum thickness prior to the base. All walls, including the outer wind tunnel walls were modeled as no-slip surfaces.

The pressure across the base is plotted and compared against the experimental values in Figure 19. Average values of the base pressure are calculated and compared to the experimental value in Table 9. The agreement is substantially better for the models with compressibility corrections (KW, BSL-CC, and SST-CC).

Figures 20 through 23 present streamwise and transverse velocities at two stations downstream of the base. These velocity profiles agree extremely well with those calculated by Suzen et al. [24], showing a grid- and code- independent solution (For SA and all of Menter's models).

Model	$\overline{P}$	% diff
Experiment	13,800 Pa	—
SA	3,380 Pa	75.5%
KW	11,100 Pa	19.5%
BSL	5,500 Pa	60.0%
SST	7,290 Pa	47.2%
BSL-CC	11,900 Pa	13.76%
SST-CC	12,300 Pa	11.1%

Table 9 2-D Base – Average base pressure compared to the experimental data

M_∞	2.46
ρ_∞	$0.7549 \frac{kg}{m^3}$
p_∞	$3.1415 \cdot 10^4 \frac{N}{m^2}$
T_∞	$145K$
Re	$\frac{45 \cdot 10^6}{m}$
R	$31.75mm$
$U_\infty = U_0$	$593.8 \frac{m}{sec}$

Table 10 Test Conditions for the axisymmetric base flow

Axisymmetric Base Flow

The experimental conditions for the axisymmetric base of Herrin and Dutton [18] were matched to test the models on high-speed axisymmetric base flows. Freestream conditions of M=2.46 and a unit Reynolds number of 45 million per meter were imposed as inflow. With a base radius of 31.75mm, the resulting Reynolds number based on the diameter was $2.858 \cdot 10^6$. The test conditions are summarized in Table 10.

The grids used are shown in Figure 24 (comparing the Quad and Tri grid). The length of the cylinder was determined in a similar fashion as the 2-D base, to provide the correct boundary layer momentum thickness prior to the base.

The base pressure for all models on the Quad grid is shown in Figure 25. Like the 2-D base, the models with compressibility corrections provide the best results. The calculated coefficient of pressure shows large variations across the base, in contrast to the flat profile in the experimental data. A refined quadrilateral grid (**Fine**) was created that had twice the number of points in the streamwise and transverse directions. Results on this grid and the Tri grid are compared in Figure 26. There are small differences in the pressure profiles, with the Fine grid results falling in between the Quad and Tri grids. Table 11 gives an average base pressure coefficient and compares to the experimental data. The models with compressibility corrections are all within 12% of the experimental value, while the SA model is over 85% off.

Model	$\overline{C_p}$	% diff
Experiment	-0.102	—
SA Quad	-0.192	88.2%
KW Quad	-0.113	10.8%
BSL Quad	-0.141	38.2%
SST Quad	-0.141	38.2%
BSL-CC Quad	-0.114	11.8%
SST-CC Quad	-0.113	10.8%
SA Tri	-0.195	91.2%
KW Tri	-0.106	3.9%
BSL-CC Tri	-0.107	4.9%
SA Fine	-0.197	93.1%
BSL-CC Fine	-0.111	8.8%

Table 11 Axisymmetric Base – Average base coefficient of pressure compared to the experimental data

Figures 27 and 28 plot velocity along the centerline (or axis of symmetry). The models with compressibility corrections provided a more reasonable separation bubble size than those without. The peak reverse velocity and location are poorly predicted by all models. This suggest that the physics of the flow is not being accurately captured. The models are adequate for engineering predictions of drag, however, since they capture the base pressure well.

NACA 0012

A NACA 0012 airfoil was run at the following flow conditions: $M_\infty = 0.799$, angle-of-attack of $\alpha = 2.86°$ and a Reynolds number based on chord of 9.0×10^6. Results were then compared to the experiments of Harris [25].

The Quad grid is shown in Figure 29. Figure 30 shows coefficient of pressure vs. chordwise distance for all models on the Quad grid. The SA and SST do a good job of predicting the shock location, while the other models predict a shock too far aft. The compressibility corrections have also been included for the SST model, and are seen to move the shock slightly upstream. Figure 31 compares the Quad grid to the Tri grid for three of the models. The shock in each case moves slightly forward and is a little more gradual. The effect seems weaker in the case of the SST model.

Axisymmetric Bump

The axisymmetric bump of Bachalo and Johnson [26] is a popular transonic shock separated test case. The experiments were run at several Mach numbers. The current computations were performed at M=0.875.

The grid is shown in Figure 32. Figure 33 plots coefficient of pressure vs. chordwise distance for all models. The SST model provides an excellent match for the shock location, and downstream behavior of C_p. All other models provide a shock location too far downstream. The SA model provides slightly better predictions of the downstream behaviour of C_p than the remaining models. The compressibility correction for the SST model was seen to have a negligible impact on the solution.

Compression Corner

The final test case was the 24° compression corner with an incoming turbulent boundary layer. The conditions for Settles' experiment [19, 20, 21] were used. The freestream Mach number is 2.85 with a velocity of 1875 ft/sec. Forsythe et al. [22] calculated this flow previously with the same turbulence models except for KW.

Results will be normalized by the boundary layer thickness at station 1 ($\delta_0 = 0.83\,\text{inch}$). A thick, fully turbulent boundary layer was imposed at the inflow in order to match the momentum thickness at station 1. The profile was generated using EDDYBL [5], and was specified by a user coded boundary condition. The Reynolds number based on δ_0 is 1.33×10^6. The freestream temperature is 180° R, with a constant wall temperature of 498° R. Settles provided surface skin friction, surface pressures, boundary layer velocity profiles at several stations, pressure contours, and Mach number contours. The grid for this case is shown in Figure 34, and is the finest grid used in [22]. A grid refinement study was performed in [22], with a coarser grid providing a grid independent solution. There is an extremely close agreement with Forsythe et al. [22], showing a code-independent solution. Figures 35 plots pressure vs. distance from the corner. The most realistic separation shock locations are given by KW and BSL-CC. The effect of turning off the compressibility corrections in the k-ω model is seen (KW-NOCC). In all cases, the compressibility correction moves the separation shock further forward. It is interesting to note that the SST model does very poorly for this flow, even though it has been successful for transonic shock separated flows. Figure 36 shows the skin-friction for the models. There is a larger distance between the separation shock and the separation location in the experiments than in the computations. This is most likely due to the unsteady shock oscillations present in the experiments, as discussed by Dolling [27].

Conclusions

An extensive testing of all turbulence models in *Cobalt*$_{60}$ was conducted. Comparisons were made to empirical data, other computational studies, and experimental data in order to validate proper implementation, robustness, model performance, and accuracy issues on triangular grids.

All models have been rigorously tested for proper implementation, showing code-independant solutions in several cases. A detailed grid refinement study on a flat plate was accomplished to explore the sensitivity to streamwise, and wall-normal spacing. The study of incompressible shear layers should be completed in the future. All models were found to be robust on all cases, handling a CFL of one million.

The model performance was tested on a wide range of problems that emphasized supersonic and transonic applications. The compressibility corrections to Menter's models either had no effect in the cases where they were expected to be passive, or improved the results. In particular the compressibility corrections were particularly successful for the base and supersonic jet flows. For these reasons the corrections will be included by default in the next release version of the code. The SST model seems to be the best overall model (for the included applications), except for the supersonic compression corner. The BSL model handles all of the supersonic cases as well as SST model, and is more accurate for the compression corner. For this reason, the BSL model will be included as a separate option, and should be considered for supersonic cases. Wilcox's k-ω model gives similar results to the BSL model for most cases, but does poorly for the supersonic round jet – even with the round jet correction activated. The cause may be sensitivity to freestream conditions, and should be further explored. The model does have the advantage of not requiring a wall distance. This may become more important for moving grid applications, where the wall distance calculation would be cost prohibitive. The SA model faired poorly in the applications with compressible shear layers, since it does not have compressible shear layer corrections. For the transonic separated cases it was the next best model behind Menter's SST. It should be kept in mind that that the cases run placed an emphasis on applications where the new models were expected to shown an advantage over the SA model.

Finally, accuracy issues were examined on triangular grids. More work is needed in the area of constructing a smooth $\mathcal{D}$-limiter, or in constructing a conservative, positive, *and* linearity preserving formulation of $\mathcal{D}$. It should be emphasized that a utility called *Blacksmith* is available that can recombine tetrahedrons in the boundary layer into prisms for grids produced by VGRIDns [4]. Also, Gridgen is currently able to grow boundary layer prisms and output *Cobalt*$_{60}$ grids [28].

Acknowledgements

The author would like to express his thanks for the advice, past efforts, and support of Dr. Yildirim Suzen. Thanks also to Dr. Paul Schuricht and Capt. Doug Blake of the USAF Academy, who were very helpful in producing this paper. Most of the computations were run on the Beowulf cluster at the USAF Academy High Performance Computing Facility.

References

[1] Strang, W.Z., Tomaro, R.F, Grismer, M.J., "The Defining Methods of Cobalt$_{60}$: a Parallel, Implicit, Unstructured Euler/Navier-Stokes Flow Solver," *AIAA 99-0786,* January 1999.

[2] Grismer, M.J., Strang, W.Z., Tomaro, R.F. and Witzemman, F.C., "Cobalt: A Parallel, Implicit, Unstructured Euler/Navier-Stokes Solver," *Advances in Engineering Software*, Vol. 29, No. 3-6, pp. 365—373, 1998.

[3] Tomaro, R.F., Strang, W.Z., and Sankar, L.N., "An Implicit Algorithm for Solving Time Dependant Flows on Unstructured Grids," *AIAA 97-0333*, January 1997.

[4] Pirzadeh, S., "Three-Dimensional Unstructured Viscous Grids by the Advancing-Layers Methods," AIAA Journal, Vol. 34, No. 1, 1996, pp. 257-265.

[5] Wilcox D.C., *Turbulence Modeling for CFD*, Second Edition, DCW Industries, Inc., 1998.

[6] Baldwin, B.S., Barth, T.J., "A One-Equation Turbulence Transport Model for High Reynolds Number Wall-Bounded Flows," *NASA TM 102847*, August 1990.

[7] Menter, F.R., "Improved Two-Equation k-ω Turbulence Models for Aerodynamic Flows," *NASA-TM-103975*, October 1992.

[8] Forsythe, J.R.,Hoffmann, K.A., Suzen, Y.B., "Investigation of Modified Menter's Two-Equation Turbulence Models for Supersonic Applications." *AIAA 99-0873*, January 1999.

[9] Menter, F.R., "Influence of Freestream Values on k-ω Turbulence Model Predictions," *AIAA Journal*, Vol 30, No 6, 1991, pp 1657–1659.

[10] Menter, F.R., "Zonal Two Equation k-ω Turbulence Models for Aerodynamic Flows," *AIAA 93-2906*, 1993.

[11] Menter, F.R., "Two-Equation Eddy-Viscosity Turbulence Models for Engineering Applications," *AIAA Journal*, Vol 32, No 8, August 1994, pp 1598–1605.

[12] Spalart, P.R., and Allmaras, S.R., "A One-Equation Turbulence Model for Aerodynamic Flows," *AIAA-92-0439*, January 1992.

[13] Hopkins, Edward J., Inouye, Mamoru, "An Evaluation of Theories for Predicting Turbulent Skin Friction and Heat Transfer on Flat Plates at Supersonic and Hypersonic Mach Numbers," AIAA Journal V. 9, No. 6, Pp 993–1003, June 1971.

[14] Barth, T.J., "Numerical Aspects of Computing Viscous High Reynolds Number Flows on Unstructured Meshes," *AIAA 91-0721,* Jan 1991.

[15] Coirier, W.J., "An Addaptively-Refined, Cartesian, Cell-Based Scheme for the Euler and Navier-Stokes Equations," *NASA TM 106754*, Oct 1994.

[16] Seiner, J. M., Norum, T. P., "Experiments of Shock Associated Noise on Supersonic Jets," AIAA 79-1526, July 1979.

[17] Suzen, Y. B., Hoffmann, K. A., "Investigation of Supersonic Jet Exhaust Flow by One- and Two-Equation Turbulence Models," AIAA 98-0322, January 1998.

[18] Herrin, J.L., Dutton, J.C., "Supersonic Base Flow Experiments in the Near Wake of a Cylindrical Afterbody," *AIAA Journal*, Vol. 32, No1, Jan 1994.

[19] Settles, G.S. "An Experimental Study of Compressible Turbulent Boundary Layer Separation at High Reynolds Numbers," PhD Dissertation, Princeton University, 1975.

[20] Settles, G.S., Vas, I.E., and Bogdonoff, S. M., "Details of a Shock-Separated Turbulent Boundary at a Compression Corner," AIAA Journal, Vol. 14, No 12, Dec. 1976, pp 1709–1715.

[21] Settles, G. S., Fitzpatrick, T. J., and Bogdonoff, S. M., "Detailed Study of Attached and Separated Compression Corner Flowfields in High Reynolds Number Supersonic Flow," AIAA Journal, Vol 17, No 6, June 1979, pp 579–585.

[22] Forsythe, J. R., Hoffmann, K., and H.-M. Damevin, "An Assessment of Several Turbulence Models for Supersonic Compression Ramp Flow," AIAA 98-2648, June 1998.

[23] Amatucci, V. A., Dutton, J. C., Kuntz, D. W., and Addy, A. C., "Two Stream, Supersonic Wake Flowfield Behind a Thick Base, Part I: General Features," AIAA Journal, Vol 30, No 8, August 1992, pp 2039–2046.

[24] Suzen, Y. B., Hoffmann, K. A., Forsythe, J. R., "Application of Several Turbulence Models for High Speed Shear Layer Flows," AIAA 99-0933, January 1999.

[25] Harris, C.D., "Two-Dimensional Aerodynamic Characteristics of the NACA 0012 Airfoil in the Langley 8-foot Transonic Pressure Tunnel," NASA TM, 81927, Apr 1981.

[26] Bachalo, W.D., and Johnson, D.A., "An Investigation of Transonic Turbulent Boundary Layer Separation Generated on an Axisymmetric Flow Model," AIAA 79-1479, 1979.

[27] Dolling, D.S., "Unsteady Phenomenona in Shock Wave/Boundary Layer Interaction," Special Course on Shock-Wave/Boundary-Layer Interactions in Supersonic and Hypersonic Flows, AGARD-R-792, Aug 1993.

[28] Steinbrenner, J., Wyman, N., Chawner, J., "Development and Implementation of Gridgen's Hyperbolic PDE and Extrusion Methods," AIAA 00-0679, Jan 2000.

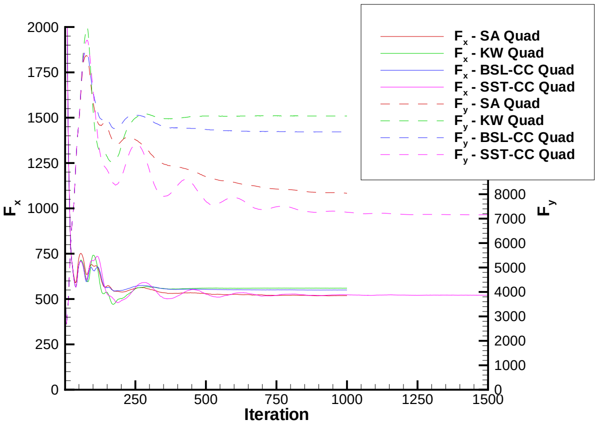

Fig. 1 Convergence history for NACA 0012 case– Axial and Normal force vs. iteration – Quad grids

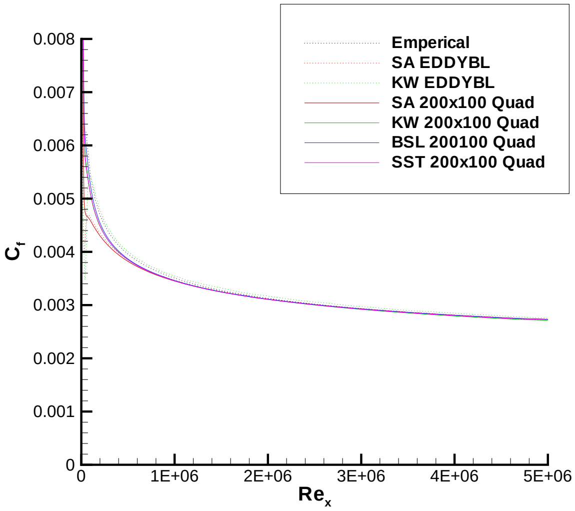

Fig. 2 Flat Plate, M=0.1 – Skin Friction vs. local Reynolds number – Quad grids

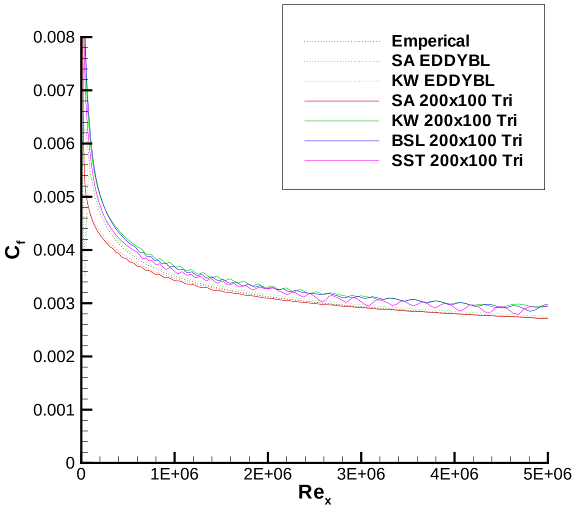

Fig. 3 Flat Plate, M=0.1 – Skin Friction vs. local Reynolds number – Tri grids

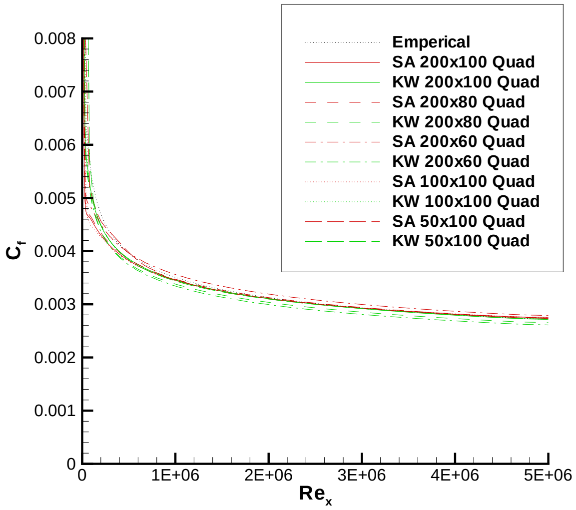

Fig. 4 Flat Plate, M=0.1 – Skin Friction vs. local Reynolds number – Quad grid refinement

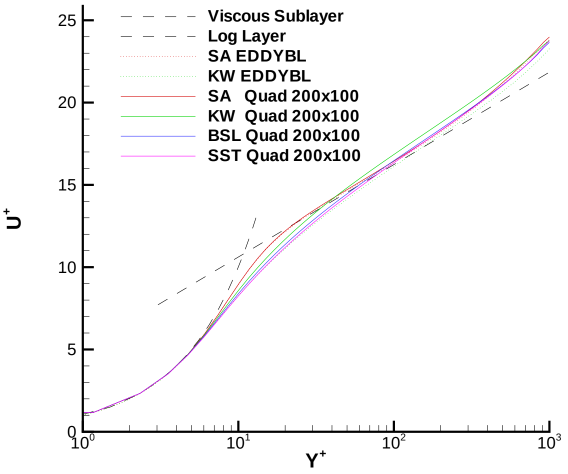

Fig. 6 Flat Plate, M=0.1 – Velocity profile at $Re_x = 2.5 \cdot 10^6$ – Quad grids

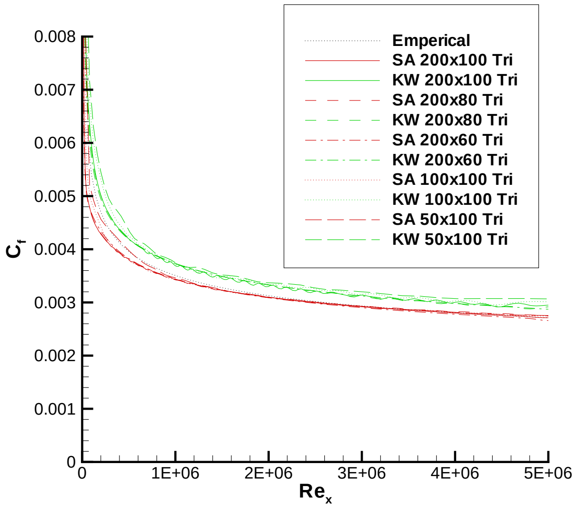

Fig. 5 Flat Plate, M=0.1 – Skin Friction vs. local Reynolds number – Tri grid refinement

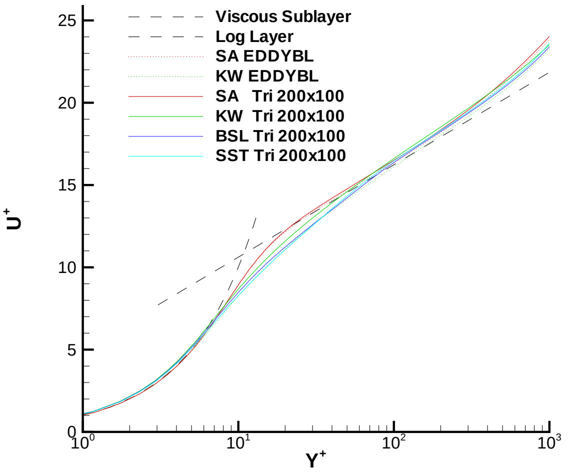

Fig. 7 Flat Plate, M=0.1 – Velocity profile at $Re_x = 2.5 \cdot 10^6$ – Tri grids

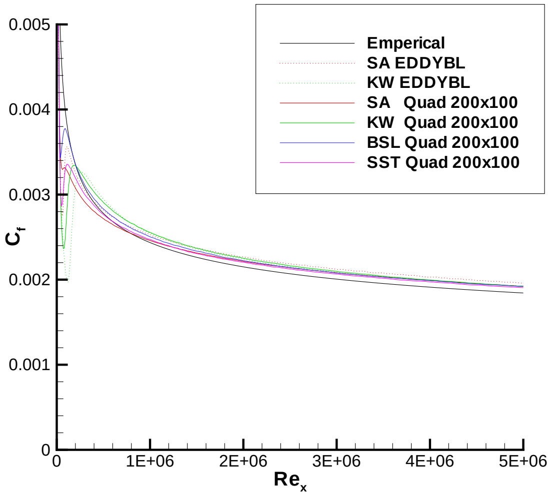

Fig. 8 Flat Plate, M=2.5 – Skin Friction vs. local Reynolds number – Quad grids

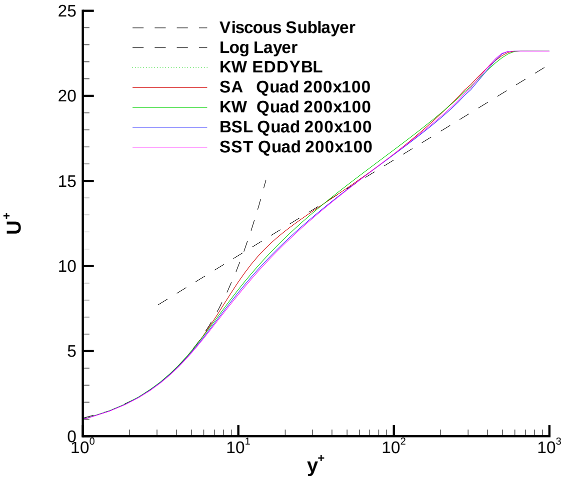

Fig. 10 Flat Plate, M=2.5 – Velocity profile (Van-Driest transformed) at $Re_x = 2.5 \cdot 10^6$ – Quad grids

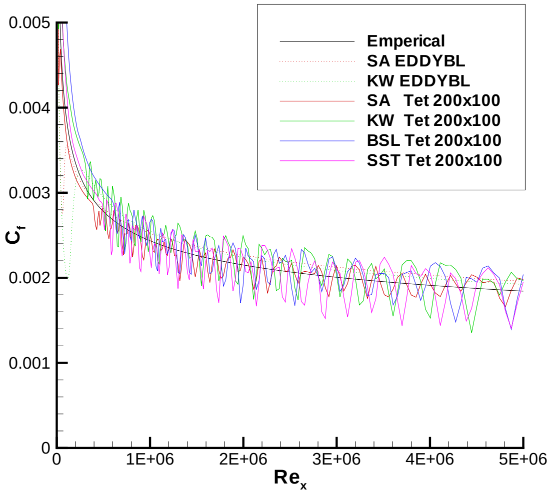

Fig. 9 Flat Plate, M=2.5 – Skin Friction vs. local Reynolds number – Tri grids

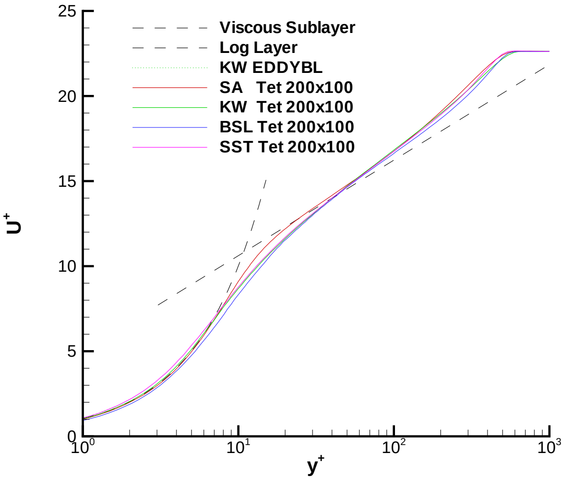

Fig. 11 Flat Plate, M=2.5 – Velocity profile (Van-Driest transformed) at $Re_x = 2.5 \cdot 10^6$ – Tri grids

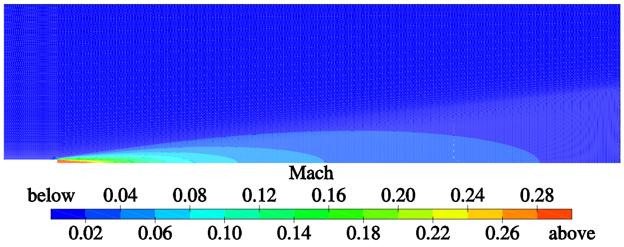

Fig. 12 Incompressible Round Jet – BSL/SST Mach contours

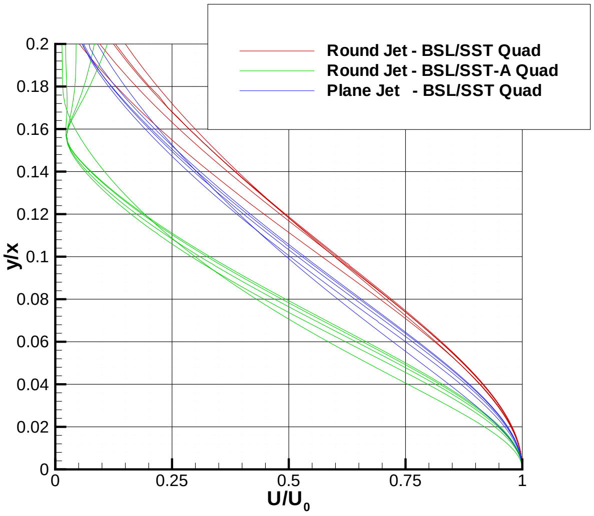

Fig. 13 Incompressible Round and Plane Jet – Velocity profiles at x=0.25,0.50,0.75,1.0,1.25 m – BSL/SST Quad grids

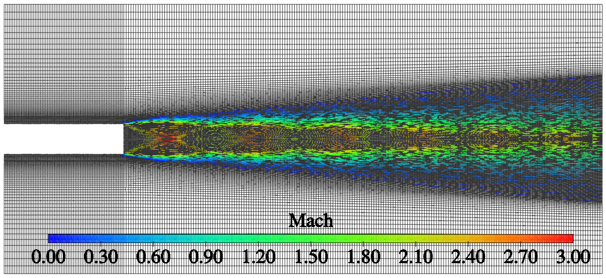

Fig. 14 Supersonic Round Jet Quad Grid – with BSL-CC Mach contours, mirrored across the plane of symmetry

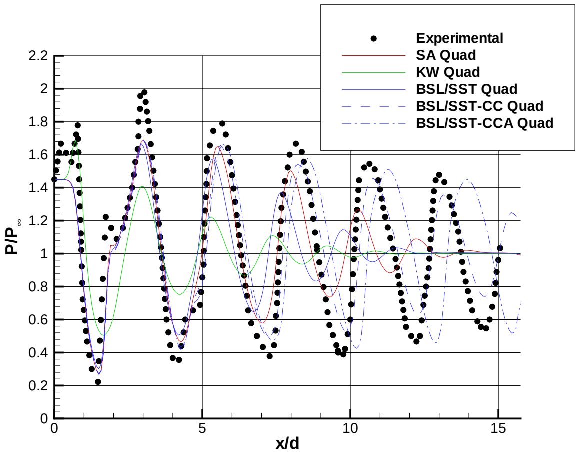

Fig. 15 Supersonic Round Jet – Pressure vs. streamwise distance along the axis of symmetry – all models

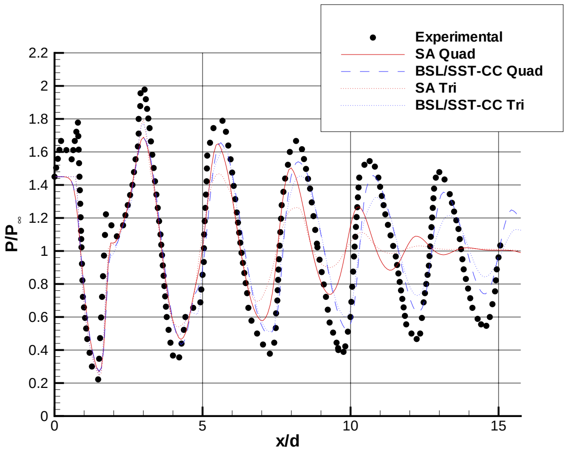

Fig. 16 Supersonic Round Jet – Pressure vs. streamwise distance along the axis of symmetry – Quad grid vs. Tet grid

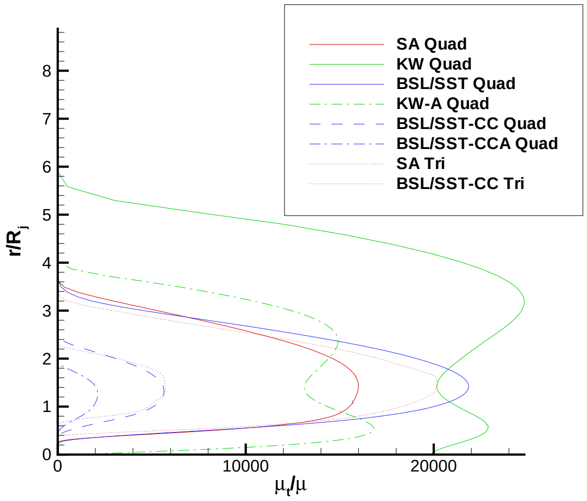

Fig. 17 Supersonic Round Jet – Non-dimensional turbulent viscosity vs. radial distance at $\frac{x}{D} = 5.5$

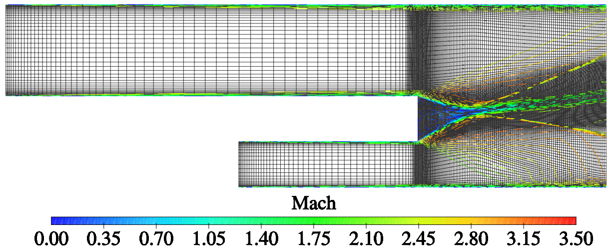

Fig. 18 2D Base Quad grid – with k-ω Mach contours

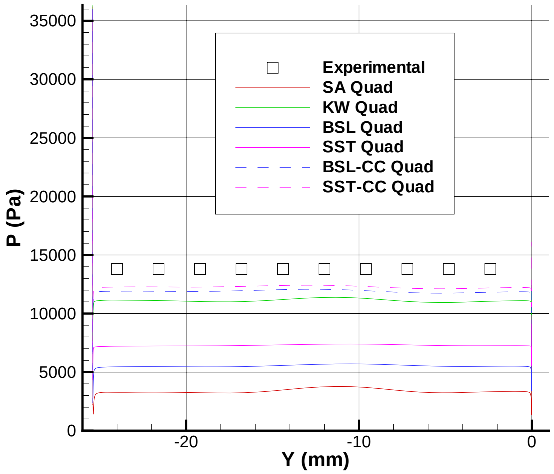

Fig. 19 2D base – Pressures on the base – all models

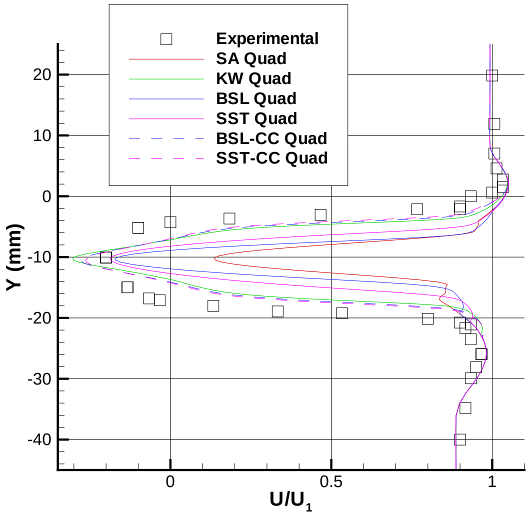

Fig. 20 2D base – Streamwise velocity, 15mm behind the base

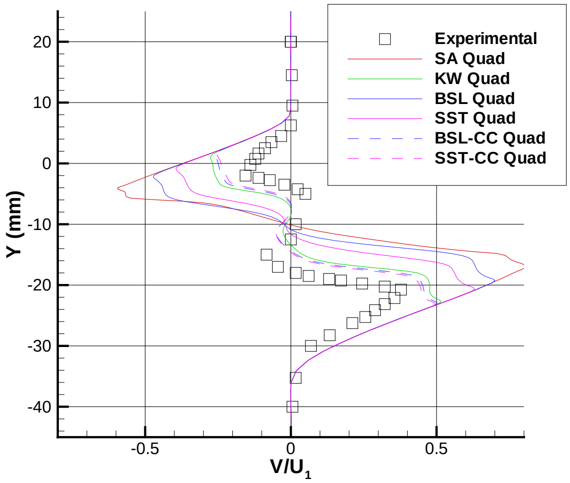

Fig. 21 2D base – Transverse velocity, 15mm behind the base

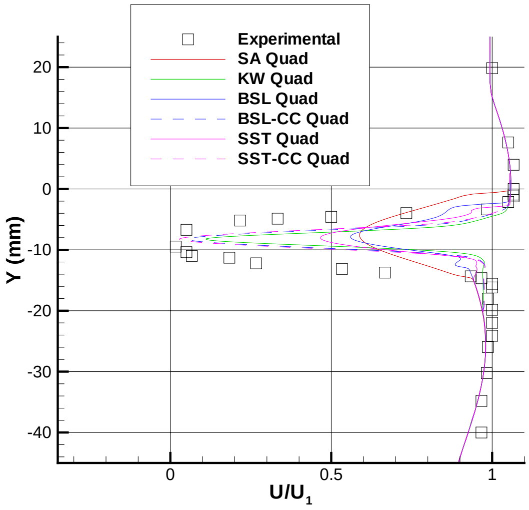

Fig. 22 2D base – Streamwise velocity, 35mm behind the base

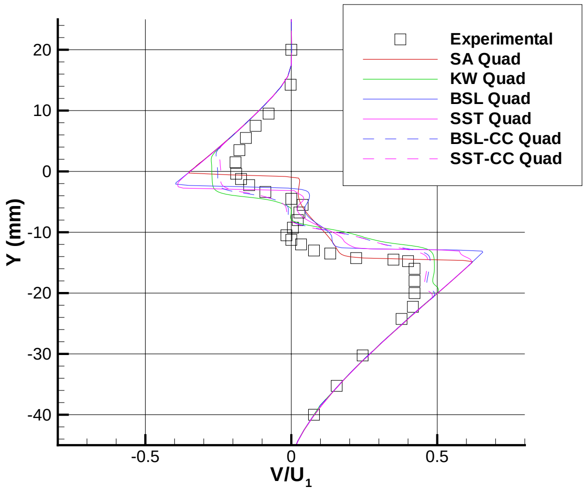

Fig. 23 2D base – Transverse velocity, 35mm behind the base

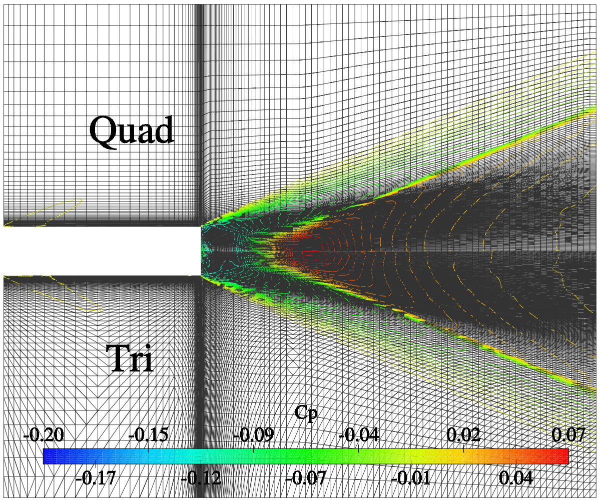

Fig. 24 Axisymmetric Base – Comparison of Quad and Tri grid across the axis of symmetry. C_p contours shown for BSL-CC

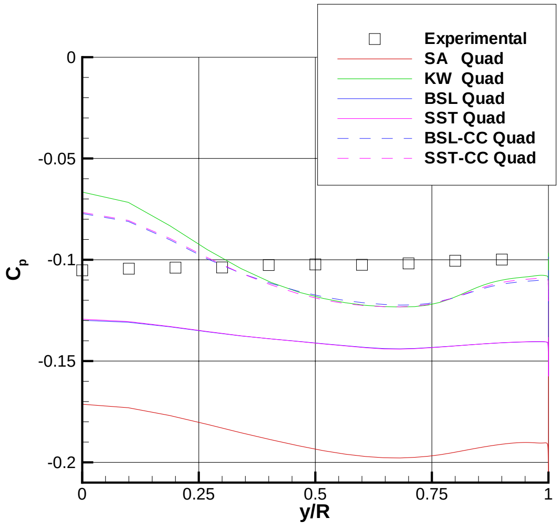

Fig. 25 Axisymmetric Base – C_p across the base – all models

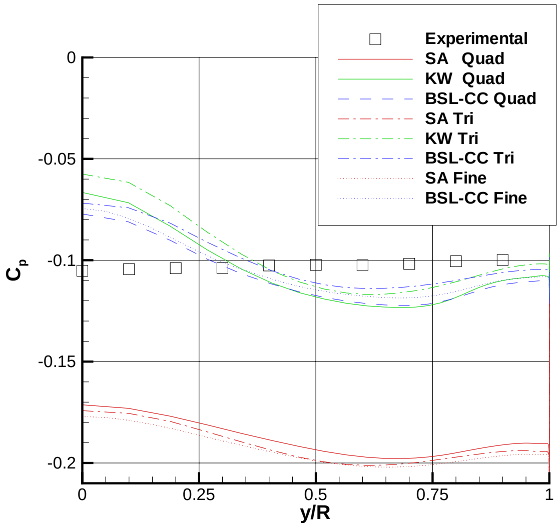

Fig. 26 Axisymmetric Base – C_p across the base – comparing Tri and Fine grids

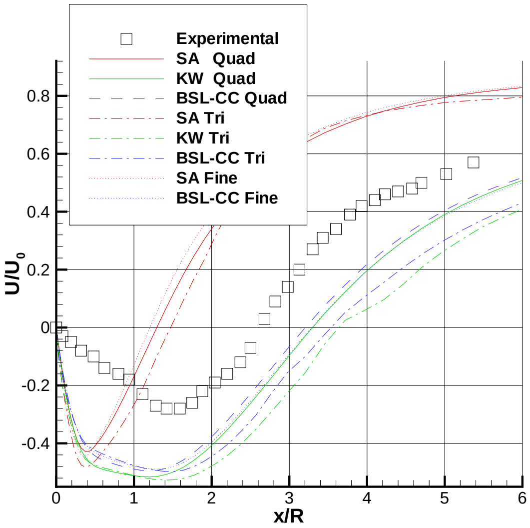

Fig. 28 Axisymmetric Base – Streamwise velocity along the cenerline – comparing Tri and Fine grids

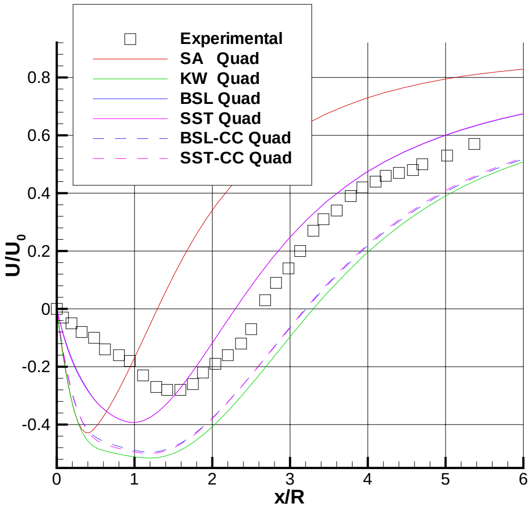

Fig. 27 Axisymmetric Base – Streamwise velocity along the cenerline – all models

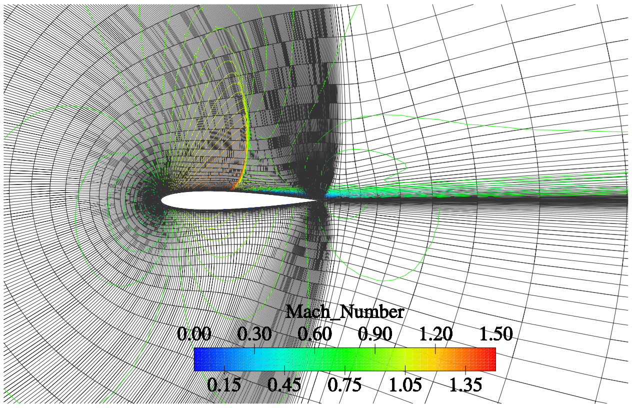

Fig. 29 NACA 0012 Quad grid – with SST-CC Mach contours

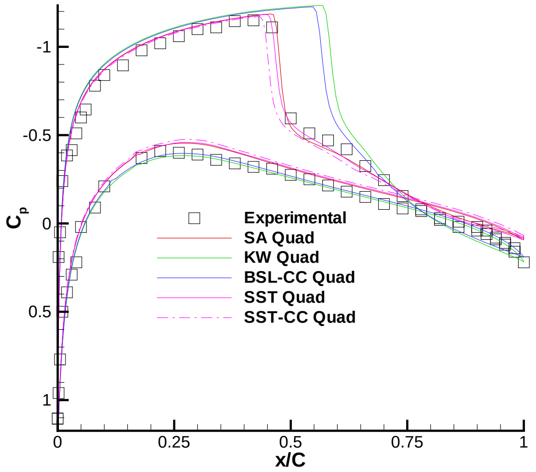

Fig. 30 NACA 0012 – C_p vs. chordwise distance – all models on the Quad grid

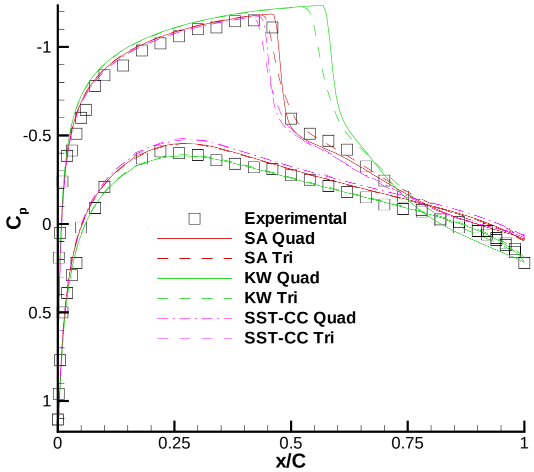

Fig. 31 NACA 0012 – C_p vs. chordwise distance – Quad grid vs. Tet grid

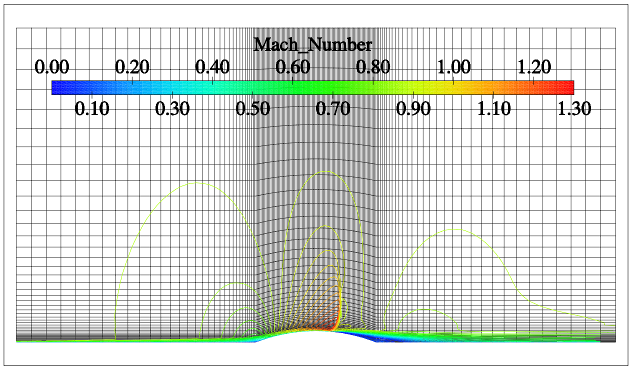

Fig. 32 Axisymmetrix Bump Quad grid – with SST Mach contours

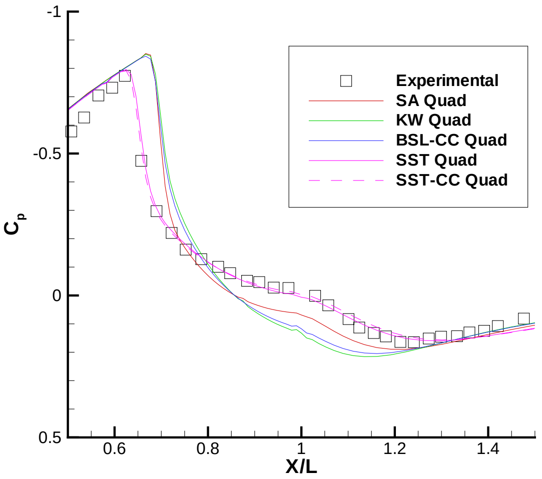

Fig. 33 Axisymmetrix Bump – C_p vs. chordwise distance

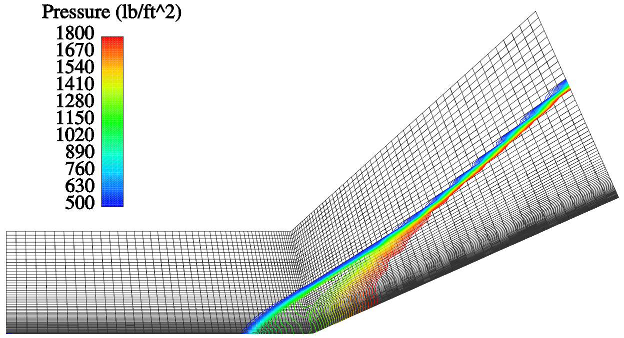

Fig. 34 **Compression Corner – Quad Grid with Pressure contours for BSL-CC**

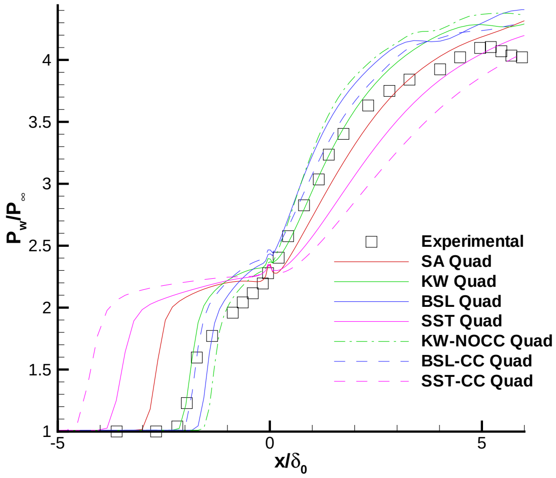

Fig. 35 **Compression Corner – Pressure vs. distance from the corner – all models**

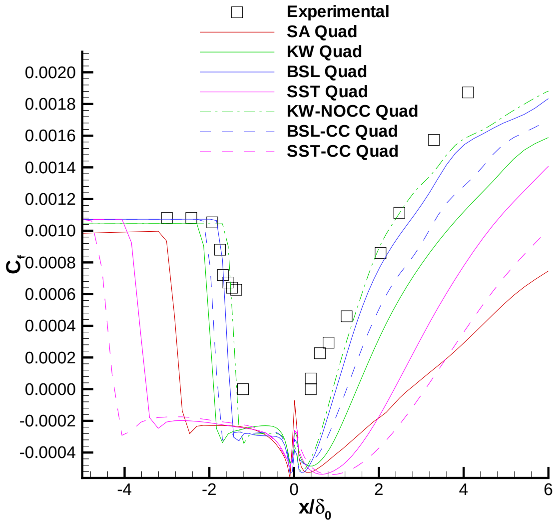

Fig. 36 **Compression Corner – Skin friction coefficient vs. distance from the corner – all models**